

# Spin-orbit coupling driven superfluid states in optical lattices at zero and finite temperatures

Kuldeep Suthar,<sup>1</sup> Pardeep Kaur,<sup>2</sup> Sandeep Gautam,<sup>2</sup> and Dilip Angom<sup>3,4</sup>

<sup>1</sup>*Institute of Atomic and Molecular Sciences, Academia Sinica, Taipei 10617, Taiwan*

<sup>2</sup>*Indian Institute of Technology Ropar, Rupnagar - 140001, Punjab, India*

<sup>3</sup>*Physical Research Laboratory, Ahmedabad - 380009, Gujarat, India*

<sup>4</sup>*Department of Physics, Manipur University, Canchipur - 795003, Manipur, India*

(Dated: October 12, 2021)

We investigate the quantum phase transitions of a two-dimensional Bose-Hubbard model in the presence of a Rashba spin-orbit coupling with and without thermal fluctuations. The interplay of single-particle hopping, strength of spin-orbit coupling, and interspin interaction leads to superfluid phases with distinct properties. With interspin interactions weaker than intraspin interactions, the spin-orbit coupling induces two finite-momentum superfluid phases. One of them is a phase-twisted superfluid that exists at low hopping strengths and reduces the domain of insulating phases. At comparatively higher hopping strengths, there is a transition from the phase-twisted to a finite momenta stripe superfluid. With interspin interactions stronger than the intraspin interactions, the system exhibits phase-twisted to ferromagnetic phase transition. At finite temperatures, the thermal fluctuations destroy the phase-twisted superfluidity and lead to a wide region of normal-fluid states. These findings can be observed in recent quantum gas experiments with spin-orbit coupling in optical lattices.

## I. INTRODUCTION

The spin-orbit interaction plays a key role in several areas of condensed matter physics and material science like topological insulators and superconductors [1–3], quantum Hall effects [4], spin liquids [5], Weyl semimetal [6], and spintronics based devices [7]. Recent advances in ultracold quantum gas experiments have allowed the implementation of spin-orbit coupling (SOC) and competing interactions in strongly-correlated many-body systems [8–10]. These experimental developments afford the possibilities to study novel states of matter, phase transitions, and exotic spin models which are not accessible in conventional condensed matter systems [11, 12]. The ultracold atomic systems are ideal platforms for such studies due to the tunability of potentials and multiparticle interactions.

In condensed matter systems, the SOC is an intrinsic property and can not be tuned [2]. In contrast, it is possible to vary the strength of synthetic SOC in ultracold atoms by tuning the Raman coupling between pseudospin states and thereby different phase transitions can be explored [13–15]. These experiments consider an equal-strength mixture of Rashba and Dresselhaus SOC. However, the experimental schemes to realize pure Rashba SOC in ultracold quantum gases have also been proposed [16]. A spin orbit-coupled pseudospin-1/2 Bose gas undergoes two successive magnetic phase transitions as the strength of Raman coupling is increased. First transition is from a stripe to a magnetized plane-wave phase, and second is from the magnetized plane-wave to a non-magnetic zero-momentum superfluid state for the Raman coupling of the order of the recoil energy [17]. Furthermore, a two-dimensional (2D) SOC exhibits inversion and  $C_4$  symmetries, thus opening new avenues to study topological band structures and quantum effects. The interaction-driven quantum phase transition and topological region of such a 2D system are explored in a recent experiment [9]. These experimental advances have led to several theoretical studies. The magnetic ordering such as spin-spiral ordering [18], vortex and Skyrmion crystal [12], and ferromagnetic and antiferromagnetic phases [19]

have been examined. The effects of strength and symmetry of SOC on the ground-state [20], crystal momentum distributions [21], and SOC-driven Mott insulator (MI) to superfluid (SF) phase transition [22] have also been investigated. The strong Rashba SOC destroys insulating domain and generates finite-momentum and stripe ordered superfluids [12, 23, 24]. The SOC-driven twisted superfluid states of binary spin mixtures in hexagonal optical lattice are also observed in quantum gas experiment [25]. The introduction of optical lattice potential breaks the Galilean invariance [26] and enhances the contrast, life-time, and parameter regime of the stripe superfluid state [27]. In spite of several studies, the parameter regions of the superfluid states in spin-orbit coupled Bose-Hubbard model and the effects of thermal fluctuations on the transition between finite-momentum superfluids have not been investigated. At finite temperatures, the melting of stripe superfluid phase leads to a wide domain of stripe normal-fluid (NF) phase [28]. More recently, it has been shown that the SOC leads to the lowering of the critical temperature for the superfluid to NF phase transition, and reduces the coherence and spatial orders of magnetic textures [29].

In the present work, we study the ground-state phase diagrams of two-component interacting bosons in the presence of Rashba SOC at zero and finite temperatures. We examine the quantum phase transitions and characterize the SOC-driven finite-momentum superfluid states in two different regimes based on the interspin interactions. For interspin interactions weaker than the intraspin interactions, the two finite momenta superfluids are phase-twisted (PT) and stripe (ST) superfluids whereas for interspin interactions stronger than intraspin interactions, these are PT and  $z$ -polarized ferromagnetic (zFM) superfluid phase. At  $T = 0\text{K}$ , the critical hopping of MI to PT superfluid transition decreases with SOC, which is in agreement to the mean-field predictions. In contrast to the condensed matter systems, the phase diagrams of the system can be explored by tuning the experimental parameters. Furthermore, we extend our study to the case of finite-temperature, and show the interplay of SOC and thermal fluctuations on the superfluid states. We observe the melting of PT superfluid

state into insulator and NF phase at finite temperatures.

The paper is structured as follows: we introduce the model Hamiltonian of the present study and provide a brief description of the mean-field Gutzwiller approach in section II. In section III, we provide the characterization of the superfluid states of the model considered. In section IV, we first discuss the zero temperature phase diagrams of the Bose-Hubbard model in the presence of synthetic SOC, and then we examine the effects of finite-temperature on the SOC-driven superfluid states. Finally we conclude our findings in section V.

## II. MODEL AND METHOD

We consider a pseudospinor system of ultracold bosons loaded into a square optical lattice. The two different atomic hyperfine levels of same atomic species act as two pseudospin states. The system is well described by a two-component Bose-Hubbard model (BHM) in the presence of Rashba SOC on a 2D optical lattice. The Hamiltonian of the system is [22]

$$\begin{aligned} \hat{H} = & -J \sum_{\langle i,j \rangle} \hat{\Psi}_i^\dagger \hat{\Psi}_j + \sum_{i,\alpha} (\epsilon_{i\alpha} - \mu) \hat{n}_{i\alpha} \\ & + \frac{1}{2} \sum_{i,\alpha} U_\alpha \hat{n}_{i\alpha} (\hat{n}_{i\alpha} - 1) + U_{\uparrow\downarrow} \sum_i \hat{n}_{i\uparrow} \hat{n}_{i\downarrow} \\ & + i\lambda \sum_{\langle ij \rangle} \hat{\Psi}_i^\dagger \hat{\mathbf{z}} \cdot (\vec{\sigma} \times \vec{d}_{ij}) \hat{\Psi}_j + \text{H.c.}, \end{aligned} \quad (1)$$

where  $i$  is a unique combination of lattice site indices in 2D, i.e.  $i \equiv (p, q)$  with  $p$  and  $q$  as site indices along  $x$  and  $y$  directions, respectively, and  $j \equiv (p', q')$  is a neighboring site of  $i$ th site. Here  $\Psi_i = (\hat{b}_{i\uparrow}, \hat{b}_{i\downarrow})^T$  is a two-component bosonic annihilation operator at  $i$ th lattice site,  $\alpha = \uparrow, \downarrow$  denotes the pseudospin components,  $J$  is spin-independent hopping amplitude of atoms, and for the present study, we consider equal hopping amplitudes for both the components,  $\epsilon_{i\alpha}$  is the energy offset of atoms with  $\alpha$  spin due to envelope confining potential and is considered to be zero,  $\mu$  is the chemical potential,  $\hat{n}_{i\alpha} = \hat{b}_{i\alpha}^\dagger \hat{b}_{i\alpha}$  is the number operator, and  $U_\alpha (U_{\uparrow\downarrow})$  is intra-(inter-) spin on-site interaction. For the present work, we choose the intraspin interactions to be same,  $U_\uparrow = U_\downarrow = U$ . We consider  $U$  as the scaling parameter for the tunneling amplitude, chemical potential, interspin interaction, and the energy of the system. The last term represents the SOC generated by Raman lasers which can be tuned in experiments using coherent destructive hopping methods [30] and represents the hopping between neighbouring sites with a spin flip. Here  $\lambda$  is the Rashba SOC strength,  $\vec{\sigma} = (\sigma_x, \sigma_y, \sigma_z)$  is a vector of Pauli spin matrices,  $\vec{d}_{ij}$  is a lattice unit vector between two neighbouring sites, and  $\hat{\mathbf{z}}$  is a unit vector perpendicular to the lattice plane.

To study the ground state properties of the system in both strong and weak coupling limit, we use single-site Gutzwiller mean-field (SGMF) theory [31–38]. In this theory, the many-body ground state is the product of single-site states. The

Gutzwiller ansatz is

$$|\Psi\rangle = \prod_i |\psi\rangle_i = \prod_i \left( \sum_{n_\uparrow, n_\downarrow}^{N_b} c_{n_\uparrow, n_\downarrow}^i |n_\uparrow, n_\downarrow\rangle_i \right), \quad (2)$$

where  $|\psi\rangle_i$  is the single-site ground state,  $N_b$  is the number of occupation basis or maximum number of bosons corresponding to each spin state at each lattice site. Here  $|n_\uparrow, n_\downarrow\rangle_i$  is the occupation or Fock state, which is the direct product of the occupation states of both spin-components and  $c_{n_\uparrow, n_\downarrow}^i$  is the corresponding Gutzwiller coefficient of the coupled Fock state. The SF order parameter and the average occupancy are defined as  $\phi_{i\alpha} = \langle \Psi | \hat{b}_{i\alpha} | \Psi \rangle$  and  $n_{i\alpha} = \langle \Psi | \hat{n}_{i\alpha} | \Psi \rangle$ , respectively. This mean-field approach has been employed in the studies of bosons in optical lattices with synthetic magnetic field and SOC [22, 39–42]. To study the effects of thermal fluctuations at finite temperatures, we use the finite-temperature Gutzwiller theory, and a brief description is presented in the appendix.

We analyze the system in weakly-interacting limit, where  $U_\alpha \ll J$ . For this regime, the Hamiltonian, Eq. (1), in the momentum space can be written as

$$\hat{H}_{\text{kin}} = \sum_{\mathbf{k}} \begin{pmatrix} \hat{b}_{\mathbf{k}\uparrow}^\dagger & \hat{b}_{\mathbf{k}\downarrow}^\dagger \end{pmatrix} \mathcal{H}_{\mathbf{k}} \begin{pmatrix} \hat{b}_{\mathbf{k}\uparrow} \\ \hat{b}_{\mathbf{k}\downarrow} \end{pmatrix} \quad (3)$$

with

$$\mathcal{H}_{\mathbf{k}} = \begin{pmatrix} -2J(\cos k_x + \cos k_y) & 2i\lambda(\sin k_x - i \sin k_y) \\ -2i\lambda(\sin k_x + i \sin k_y) & -2J(\cos k_x + \cos k_y) \end{pmatrix}.$$

The diagonalization of the above Hamiltonian  $\mathcal{H}_{\mathbf{k}}$  yields two energy branches

$$E_{\mathbf{k}\pm} = -2J(\cos k_x + \cos k_y) \pm 2\lambda \sqrt{\sin^2 k_x + \sin^2 k_y}, \quad (4)$$

where  $\mathbf{k} = (k_x, k_y)$ , and the first term is spin-independent dispersion relation in a 2D square lattice. The energy spectrum  $E_{\mathbf{k}\pm}$  remains invariant under the parity transformation ( $k_x \rightarrow -k_x, k_y \rightarrow -k_y$ ) and permutation of  $k_x$  and  $k_y$ , ( $k_x \rightarrow k_y, k_y \rightarrow k_x$ ). The non-interacting lowest band structure is shown for two different regimes in Fig. 1. In the absence of SOC  $\lambda = 0$ , the lower branch of the band has one minimum at  $\mathbf{k} = (0, 0)$ . The SOC term modifies the band structure, where the lower branch has four degenerate minima. The presence of SOC breaks the rotational symmetry in  $\mathbf{k}$ -space and shifts the minima of the lower branch along the diagonals of the first Brillouin zone.

The four degenerate minima in the lower branch are  $\mathbf{q}_1 = (k_0, k_0)$ ,  $\mathbf{q}_2 = (-k_0, k_0)$ ,  $\mathbf{q}_3 = (-k_0, -k_0)$ ,  $\mathbf{q}_4 = (k_0, -k_0)$  where  $k_0 = \arctan(\lambda/\sqrt{2}J)$ . Hence, the location of the minima is determined by the strength of SOC.

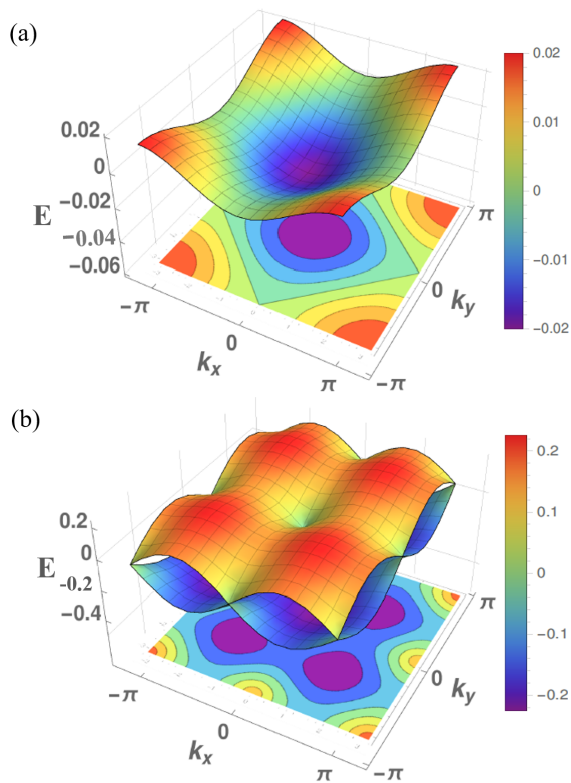


FIG. 1. Noninteracting band structure of two-dimensional square optical lattice for two regimes (a)  $\lambda/J = 0$  representing the single minima at  $\mathbf{k} = 0$  in the absence of SOC. The other case is shown for finite SOC, where the competition between  $\lambda$  and  $J$  determines the band structure. (b)  $\lambda/J = 8$ , the SOC breaks the rotational symmetry, and the minima occur at four finite wave-vectors in the lower branch. This is evident from the projection of lower energy branch onto the  $k_x$ - $k_y$  plane. As  $\lambda/J$  decreases, the minima of the lower branch tends to approach  $\mathbf{k} = 0$ .

### III. QUANTUM PHASES AND ORDER PARAMETERS

The ground states of ultracold bosons with SOC exhibit insulating and various SF phases. The nature of the SF phase depends on the competition between the single-particle hopping and SOC induced spin-dependent hopping. At lower  $J$ , the incompressible insulating phases are identified by the sum and difference of the expectations of the number operators,  $\langle \hat{n}_{\pm} \rangle \equiv \langle \hat{n}_{\uparrow} \rangle \pm \langle \hat{n}_{\downarrow} \rangle$ . For the MI phase  $\langle \hat{n}_{\pm} \rangle$  is an integer while the SF phases are characterized by real  $\langle \hat{n}_{\pm} \rangle$  and finite value of the compressibility  $\kappa = \partial \langle \hat{n} \rangle / \partial \mu$ . In the absence of SOC, the amplitude and phase of the order parameter  $\phi_{\uparrow}(\phi_{\downarrow})$  are homogeneous.

The striking features appear when the spin-dependent hopping due to the SOC is finite. This is a complex hopping, it flips the atomic spin while hopping and causes variations in the phase of SF states. To classify the various SF states which feature distinct phase distributions of the order param-

eter, we examine the spin-dependent momentum distributions at the wave vector  $\mathbf{k}$

$$\langle \rho_{\uparrow, \downarrow}(\mathbf{k}) \rangle = L^{-2} \sum_{i, j} \langle \hat{b}_{i\uparrow}^{\dagger} \hat{b}_{j\downarrow} \rangle e^{i\mathbf{k} \cdot (\mathbf{r}_i - \mathbf{r}_j)}, \quad (5)$$

where  $L$  is the system size and  $\mathbf{r}_i$  ( $\mathbf{r}_j$ ) is the location of  $i$ th ( $j$ th) lattice site. When the interspin interaction is weaker than intraspin, the SF state can be of three types. These are (i) homogeneous superfluid: this has uniform amplitude and phase of the order parameter. For this state, the condensation occurs at zero momentum and is also referred as zero-momentum SF (ZM-SF) state. (ii) Phase-twisted (PT) superfluid: for this state the amplitude of  $\langle \hat{b}_{i\alpha} \rangle$  is uniform but the phase varies diagonally across the lattice (iii) Stripe (ST) superfluid: this state has stripe-like variation in the phase of  $\langle \hat{b}_{i\alpha} \rangle$  across the lattice. Thus, we distinguish superfluid states based on their phase variation and momentum distributions. It is worth mentioning, similar SF states have been previously discussed in the continuum where the phases were characterized using the properties of collective excitations [43].

The interplay of spin-dependent hopping (SOC) and single-particle hopping leads to the exotic SF states. We examine the spin-dependent momentum distributions  $\langle \rho_{\uparrow, \downarrow}(\mathbf{k}) \rangle$  at  $\mathbf{k} = 0$ ,  $\langle \rho_{\uparrow, \downarrow}(\pm k_0, 0) \rangle$ ,  $\langle \rho_{\uparrow, \downarrow}(0, \pm k_0) \rangle$ , and  $\langle \rho_{\uparrow, \downarrow}(\mathbf{q}_i) \rangle$ . Here,  $\mathbf{q}_i$  and  $k_0$  depend on the ratio of the hopping to the SOC strength as discussed in Sec. II. For the PT superfluid, the momentum distribution at  $\langle \rho_{\uparrow, \downarrow}(\mathbf{q}_i) \rangle$  is finite either at all the  $\mathbf{q}_i$ 's or only at one of the  $\mathbf{q}_i$ 's. This is due to the variation in phase distributions along the diagonal. Hence, this state shows a peak along the diagonal of the Brillouin zone in the  $\mathbf{k}$ -space. On the other hand, for the ST superfluid states, depending on the phase variation being horizontal or vertical, the state exhibits peak at  $\langle \rho_{\uparrow, \downarrow}(\pm k_0, 0) \rangle$  or  $\langle \rho_{\uparrow, \downarrow}(0, \pm k_0) \rangle$ , respectively. We define  $\Phi = \langle \rho_{\uparrow, \downarrow}(k_0, 0) \rangle + \langle \rho_{\uparrow, \downarrow}(-k_0, 0) \rangle + \langle \rho_{\uparrow, \downarrow}(0, k_0) \rangle + \langle \rho_{\uparrow, \downarrow}(0, -k_0) \rangle$ , which serve as an order parameter to identify the PT-ST phase transition. Here,  $\Phi$  is zero for the PT superfluid while finite for the ST state. As both PT and ST are SOC-driven finite-momentum superfluid states, therefore  $\langle \rho_{\uparrow, \downarrow}(0, 0) \rangle = 0$ . In the next section, we have characterized the various phase transitions and the finite-momentum superfluids based on the aforementioned classification. Furthermore, when the interspin interaction is strong  $U_{\uparrow\downarrow} > 1$ , we also report a ferromagnetic phase where the spins orient along  $\pm z$  axis. This is referred to as  $z$ -polarized ferromagnetic (zFM) superfluid state where  $\langle \hat{b}_{i\uparrow} \rangle$  ( $\langle \hat{b}_{i\downarrow} \rangle$ ) remains finite and homogeneous but  $\langle \hat{b}_{i\downarrow} \rangle$  ( $\langle \hat{b}_{i\uparrow} \rangle$ ) vanishes throughout the lattice. This phase can be easily distinguished from other superfluid states with finite  $\phi_{\uparrow}$  or  $\phi_{\downarrow}$ .

At finite temperatures, the superfluid states are characterized in a similar way as in the case of zero temperature, although the observables are defined with the thermal averages. The definitions of the thermal-averaged SF order parameter and occupancy are provided in the appendix. The normal-fluid state at finite temperatures is identified in the incompressible phases based on the compressibility  $\kappa$ . In the present work, we consider  $|n - n_{\text{th}}| \geq 10^{-3}$  as the criterion to identify MI to NF crossover. Here,  $n$  and  $n_{\text{th}}$  are the lattice occupancies

at zero and finite temperatures, respectively. Such a criterion has been previously used to distinguish the NF phase of Bose-Hubbard model at finite temperatures [44].

#### IV. RESULTS AND DISCUSSION

We study the mean-field ground state phase diagram of the ultracold bosons and investigate the different SF phases emerging from the competition between the SOC and single-particle hopping. In particular, we examine the system for weak ( $U_{\uparrow\downarrow}/U < 1$ ) and strong ( $U_{\uparrow\downarrow}/U > 1$ ) interspin interactions. We, then, employ finite-temperature Gutzwiller theory to probe the effects of thermal fluctuations on the SF phases of the bosons. To generate the phase diagrams, we consider a system size of  $8 \times 8$ , and Fock state dimension at each lattice site is  $N_b = 6$ . The latter is sufficient to represent the quantum phases of the system upto  $\mu = 3U$  [31–34]. It is important to note that the initial states play a key role in determining the ground states. We have performed the numerical simulations with different initial states and found that a random SF order parameter as the initial state gives the global minima. The uniform  $\phi$ 's is not a good choice of the initial state because for some values of the parameters the converged solution corresponds to a local minima. This is due to the fact that the uniform  $\phi$  do not contribute to the SOC energy as this depends on the relative phase between the  $\phi$ 's of both the pseudospinor components. To obtain the mean-field phase diagrams, we start with a complex random distribution of Gutzwiller coefficients across the lattice, and then the corresponding SF order parameter is computed. Hence, our initial state has a random SF order parameter with random amplitude and phase. Our algorithm is based on the self-consistent approach. We diagonalize the single-site Hamiltonians and compute the updated  $\phi_{i\alpha}$ 's at each iteration. This process is repeated until the energy and superfluid order parameter converge upto a tolerance of  $10^{-12}$ . Moreover, we repeat the procedure with 50 random configurations of the initial state to ensure that the ground state has been obtained. We have checked explicitly that the larger number of random configurations do not modify the ground states.

##### A. $U_{\uparrow\downarrow} = 0.5$

We first examine the quantum phases of 2D BHM in the presence of SOC interaction at zero temperature. The plots in the Fig. 2 show the ground state phase diagrams at different values of the SOC strengths ( $\lambda$ 's) with  $U_{\uparrow\downarrow} = 0.5U$ .

##### 1. No spin-orbit coupling ( $\lambda = 0$ )

In the absence of SOC, the system supports two quantum phases, the incompressible MI phase and the compressible ZM-SF phase. The MI phase occurs in lobes of different integer commensurate densities. It is to be noted that the MI lobes with odd integer occupancies are smaller than those with

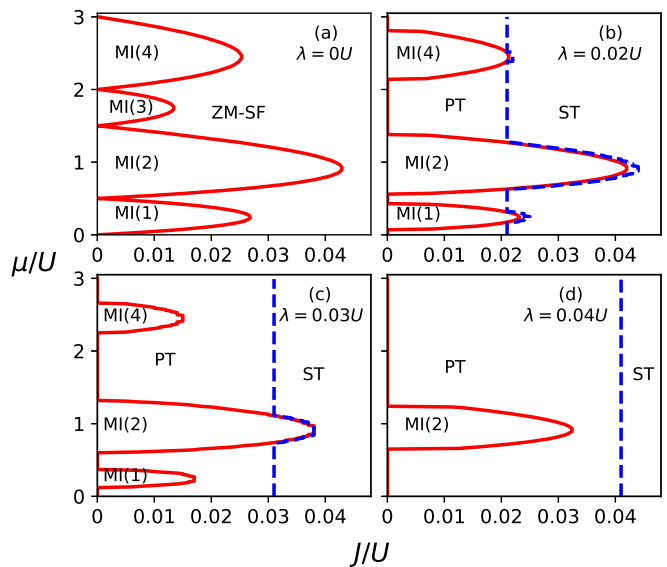


FIG. 2. The zero-temperature ground state phase diagram in the presence of Rashba SOC for various SOC strengths. The Mott insulator regime is represented by  $MI(n)$ , where  $n = n_{\uparrow} + n_{\downarrow}$  is the total filling or occupancy of the lobe. The interspin interaction  $U_{\uparrow\downarrow} = 0.5U$ , and the values of  $\lambda$  in units of  $U$  are shown in the upper right corner of the plot. At  $\lambda = 0$ , the system exhibits MI-SF transition, where the SF phase Bose condenses at zero momentum, and hence referred to as the zero momentum (ZM) superfluid state. The finite  $\lambda$  results in finite-momentum superfluid phases. Here, as  $J$  is varied the system undergo PT-ST superfluid phase transition, shown by blue dashed lines. The phase diagrams are obtained using random complex initial states with 50 random configurations. The system size  $L = 8 \times 8$  and periodic boundary conditions are considered.

even occupancies [45]. As  $U_{\uparrow\downarrow}$  increases, the size of the odd-integrated Mott lobes grow whereas even-integrated lobes remain same in size but shift to higher  $\mu/U$  until  $U_{\uparrow\downarrow} = U$ . In the absence of SOC, the phase diagram shown in Fig. 2(a) agrees well with previous studies on the two-component BHM [45–48].

##### 2. Finite spin-orbit coupling ( $\lambda \neq 0$ )

The ground state phase diagram for finite SOC are shown in Fig. 2(b)-(d). Consider the phase diagram at  $\lambda = 0.02U$ , a prominent feature is the shrinking of the MI lobes. At higher  $\mu$ , the MI(3) lobe vanishes and is replaced by the SOC-induced SF phase. Thus, even in the atomic limit  $J/U = 0$ , for certain ranges of  $\mu$ , the system is in the SF phase due to the SOC. This is evident from the phase diagram in Fig. 2(b), where the SF phase is present at  $J/U = 0$  for  $\mu/U \leq 0.07, 0.43 < \mu/U < 0.57, 1.38 < \mu/U < 2.14$  and  $2.8 < \mu/U \leq 3.0$ . In the absence of single-particle hopping i.e.  $J = 0$ , the superfluidity is due to the transport of atoms in the presence of spin-dependent hopping (SOC). As we increase  $\lambda$ , the MI lobes shrink further, and the SF phase is enhanced. For  $\lambda = 0.04U$ , only MI(2) lobe survives, and the system is in the SOC-generated SF phases in the remain-

ing parameter domain. This is due to the relatively larger region covered by MI(2) lobe even at  $\lambda = 0$ . Our computations for larger  $\lambda$  show that the MI(2) lobe also vanishes at  $\lambda \approx 0.06U$ . Hence, the MI lobe with larger insulating domain and higher  $J_c$  will require larger SOC strengths to result in superfluid states occupying the whole domain of  $J/U - \mu/U$  plane. The vanishing of insulating lobes with the formation of SOC-induced SF states is in agreement with the previous studies [22, 24]. Using site-decoupling approximation and second-order perturbation theory, the critical hopping of MI-SF transition in the presence of SOC is

$$\left(\frac{zJ_c}{U}\right) = \frac{1}{2} \left[ \left(\frac{zJ_0}{U}\right) + \sqrt{\left(\frac{zJ_0}{U}\right)^2 - 8\left(\frac{\lambda}{U}\right)^2} \right], \quad (6)$$

where  $J_0$  is the critical hopping of MI-SF transition in the absence of SOC ( $\lambda = 0$ ). The value of  $J_0$  depends on the occupation number of the species [49]. Here  $z = 2d$  is the coordination number of the  $d$ -dimensional optical lattice. The value of  $J_c$  decreases with  $\lambda$ , which confirms our numerical results in the phase diagrams shown in Fig. 2. As an illustration, for MI(2)-SF phase transition, the above expression yields the value of  $J_c$  as 0.0418 and 0.0402 for  $\lambda/U = 0.02$  and 0.03, respectively, which are in close agreement to the numerical values in phase diagrams in Figs. 2(b)-(c). Using Eq. 6, the critical SOC strengths where MI(2) and MI(4) lobes destroy are 0.061 and 0.035, respectively and these are consistent to our numerical results.

At  $\lambda = 0$ , the only superfluid phase of the system is ZM superfluid, whereas at non-zero  $\lambda$  value, it is replaced by finite-momentum superfluids. The nature of superfluid phases near the MI-SF transition can be understood by analyzing the mean-field energies [24]. The hopping energy depends on the relative phase between the same spin state while the SOC energy depends on the relative phase between different components. For  $\lambda = 0$  case, the minimization of hopping energy leads to zero phase difference between the states which corresponds to ZM superfluid [Fig. 2(a)]. For finite  $\lambda$ , the energies depend on  $\lambda/J$ , relative phases, and the ratio of the amplitude of  $\phi_\downarrow$  and  $\phi_\uparrow$ . For fixed  $\lambda/J$  and assuming uniform amplitude of order parameters, the minimization of energies with respect to relative phases correspond to finite but uniform relative phases [24], which is identified as PT superfluid state.

The characteristic properties of the finite-momentum and ZM-superfluid states are shown in Fig. 3. The phase variations and the momentum distributions of the finite-momentum superfluids are shown for fixed  $\lambda = 0.02U$ ,  $\mu = 1.5U$ , and two different  $J$  values corresponding to PT and ST superfluids. For the PT superfluid state, the random initial state yields uniform amplitude and twisted diagonal site-variation in the phase as evident from Fig. 3(a). The phase variation is shown for one of the components, although it is to be noted that the other component also follows similar distributions. However, the relative phase of the  $\phi$ 's between the components is finite, i.e.  $\theta_{i\uparrow} \neq \theta_{i\downarrow}$  [24]. In the presence of the interactions, the four-fold symmetry of lower branch of lowest energy band is spontaneously broken. For the PT superfluid phase, the sys-

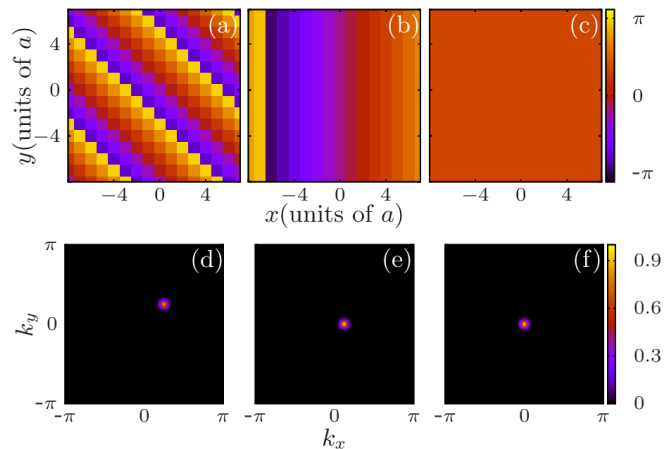


FIG. 3. The lattice-site distributions of the phase variation and spin-dependent momentum distributions of various superfluid states. The upper panel represents the phase distributions for (a) PT (b) ST (c) ZM superfluids. And, the momentum distributions are shown in the lower panel (d,e,f). The finite-momentum superfluids are obtained using the Gutzwiller mean-field approach for  $\lambda = 0.02U$  and  $\mu = 1.5U$ . The hopping amplitude in terms of  $U$  corresponding to PT and ST are 0.015 and 0.04, respectively. The ZM-superfluid (c) is plotted for  $\lambda = 0$ ,  $\mu = 1.5$ , and  $J = 0.04U$ . The spatial variation of phase and momentum distributions are shown for one of the components, as the other component also has the similar distributions. The peak in the spin-dependent momentum distributions appears at  $\mathbf{k} \neq 0$  for PT (d) and ST (e) states, whereas for ZM-superfluid it appears at  $\mathbf{k} = 0$  (f). Here,  $a$  is the lattice constant.

tem chooses to be in one of the minima and therefore, we observe a single peak at  $\mathbf{k} \neq 0$  in the momentum distribution. In particular, the peak in the  $\mathbf{k}$ -space appears at the diagonal of the Brillouin zone as represented in Fig. 3(d).

As  $J$  is increased, PT phase undergoes a transition to the ST phase. In the ST superfluid phase obtained with SGMF approach, the amplitude of  $\phi_{i\alpha}$  remains spatially uniform and phase distributions exhibit stripe-like variation [Fig. 3(b)]. The momentum peak is located at  $\mathbf{k} \neq 0$ , and in particular it lies on  $x$ - or  $y$ - axis depending on the variation in phase [Fig. 3(e)].

To examine the quantum phase transition between phase-twisted and ST superfluid state, we analyze the properties of  $\langle \rho_{\uparrow\downarrow}(\mathbf{k}) \rangle$ . Since both states are finite-momentum superfluids, their location of momentum peaks in  $\mathbf{k}$ -space can serve as an order parameter to identify them. As mentioned earlier in Sec. III, we in particular analyze the evolution of the order parameter  $\Phi$ , which is the sum of  $\langle \rho_{\uparrow\downarrow}(\mathbf{k}) \rangle$  at  $\mathbf{k} = (\pm k_0, 0)$  and  $(0, \pm k_0)$ , as a function of  $J$ . For each  $\mu$  value, we have spanned along the  $J/U$ -axis, and whenever  $\Phi$  takes a non-zero value, critical hopping strength for PT-ST transition is determined. The error involved in analyzing the phase transition is  $10^{-3}$  which is the step size ( $\Delta J$ ) used to span  $J/U$  in the numerical computations. Hence, we find that the PT-ST phase transition is sharp. As a representative case, the evolution of  $\Phi$  at  $\mu/U = 1.8$  for three different  $\lambda$  values are shown in Fig. 4. At lower hopping strengths, the ground state is either MI phase or the finite-momentum PT superfluid,

and hence  $\Phi$  remains zero. This is due to the fact that PT state corresponds to the condensation in  $\mathbf{k} = \mathbf{q}_i$  along diagonals of the first Brillouin zone. As  $J/U$  increases, a striped-ordering of the phase develops with finite  $\Phi$ , this characterizes PT-ST superfluid phase transition of the spin-orbit coupled bosons. The critical hopping strength of the PT-ST transition increases as the value of SOC strength increases. As shown in Fig. 4, the  $J_c$  of PT-ST transition is 0.02, 0.03, and 0.04 for  $\lambda = 0.02, 0.03$  and  $0.04$ , respectively. The behaviour of  $\Phi$  and the corresponding transitions for  $U_{\uparrow\downarrow} = 0.5$  [Fig. 2] suggest that the PT to ST superfluid phase transition occurs when  $\lambda/J \approx 1$ . And, the PT phase is expected for  $\lambda/J \lesssim 1$  whereas the ST phase appears for  $\lambda/J \gtrsim 1$ . Our computations using random configurations of complex  $\phi$ 's suggest an increase in  $J_c$  as the system size increases. Since the real cold-atom experiments are with the trapped finite-size systems, therefore the transition between finite-momentum superfluids can be observed near the trap-center [22].

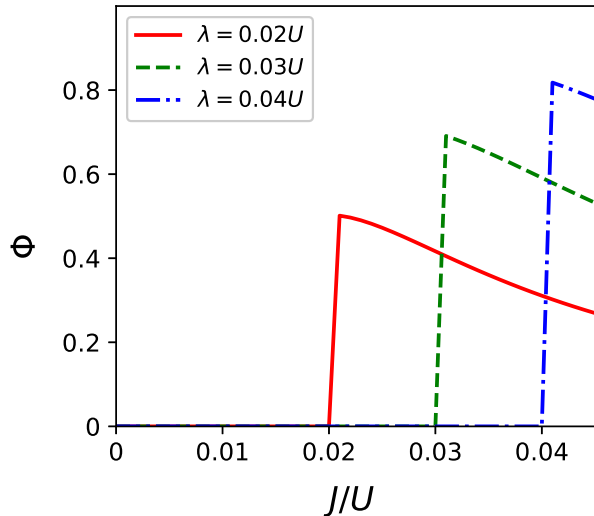


FIG. 4. The evolution of the order parameter  $\Phi$ , characterizing the finite-momentum PT (phase-twisted) and ST (stripe) superfluid states, as a function of the hopping strength  $J/U$ . The chemical potential  $\mu/U = 1.8$  and interspin interaction  $U_{\uparrow\downarrow} = 0.5U$ . The  $\Phi$  is defined in Sec. III. The variation in  $\Phi$  from zero to finite shows PT(MI)-ST phase transition.

The SGMF approach failed to capture the density oscillations that should ideally be there in a stripe phase, and the reason is that SGMF does not include the inter-site atomic correlations. In order to overcome this limitation of SGMF, and obtain the nonuniform magnetic ordering and the resulting inhomogeneous superfluidity, one has to use the diagonalization of cluster of lattice sites as suggested in Ref. [12]. Considering this, we probe the parameter space of the stripe superfluid state obtained from SGMF theory with the cluster Gutzwiller approach (CGA). The latter improves the inter-site correlations and incorporates the effects of the quantum fluctuations. In this approach, the lattice sites are partitioned into a finite number of clusters, where the model terms within the lattice sites of a cluster are treated exactly. The detailed description of the approach is given in our previous works [38, 40–42, 45].

To examine the parameter domain corresponding to the stripe superfluid, we use  $2 \times 2$  cluster and  $N_b = 3$ . The size of the clusters is sufficient to probe the effects of the atomic correlations on the magnetic ordering of the SOC-driven superfluids. Like in the case of SGMF, sometimes the solution obtained from CGA is a metastable state corresponding to a local minima. To avoid this we consider several random configurations of the SF order parameters as the initial states with CGA and choose the global minimum-energy state as the ground state phase. The lattice-site distributions of the occupancy, and the amplitude and phase of the SF order parameter are shown in Fig. 5. The profiles are shown for one of the component,  $|\uparrow\rangle$ , however the other component also follows the similar distributions. We observe the stripe variation in the number occupancy  $\langle \hat{n}_{i\alpha} \rangle$  and  $|\phi_{i\alpha}|$ , and hence term it as  $ST_{\text{den}}$  phase. The amplitude of the variations remain smaller, which we expect, can be enhanced by considering larger cluster of sites.

We further investigate the parameter domain of the stripe superfluid (using CGA) and find that the  $ST_{\text{den}}$  phase persists for larger hopping strengths. It continues to the domain where one would get ZM-SF transition using SGMF. As an example, for the parameters  $L = 8 \times 8$ ,  $\lambda = 0.02U$ ,  $\mu = 1.8U$ , and  $J = 0.1U$ , the SGMF predicts ZM-superfluidity whereas the CGA gives  $ST_{\text{den}}$  phase for these parameters. Hence, the latter extends the parameter space of  $ST_{\text{den}}$  phase by taking into account the quantum correlations. This suggests the applicability of SGMF to describe the quantum phase transitions usually for  $J/U \rightarrow 0$  [12, 22, 24]. Therefore, for the present work, we have investigated the phase transitions in the range from  $J = 0$  to  $J \approx 0.08U$ . The stability of the  $ST_{\text{den}}$  superfluid in a wider parameter regime is consistent with the observation of this state in the presence of weak lattice potential in a recent experiment [27]. In the present work, the CGA has been used to ascertain the nature of ST and ZM phases obtained from SGMF. However, the detailed analysis of the phase diagrams with CGA can be addressed in a future work.

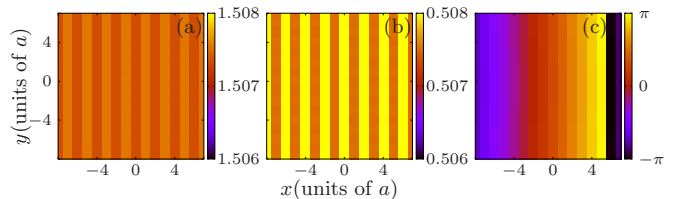


FIG. 5. The lattice-site distributions of the  $ST_{\text{den}}$  phase obtained using cluster Gutzwiller approach. (a) the occupancy (b) amplitude of the order parameter, and (c) phase of a  $ST_{\text{den}}$  state are shown. The parameters considered are  $\lambda = 0.02U$ ,  $\mu = 1.8U$ , and  $J = 0.05U$ . These distributions are shown for interspin interaction  $U_{\uparrow\downarrow} = 0.5U$ .

## B. $U_{\uparrow\downarrow} = 1.5$

Here, we discuss the quantum phases generated due to the effects of SOC when the interspin interaction is stronger than the intraspin ones ( $U_{\uparrow\downarrow}/U > 1$ ). In this parameter regime, we first review the phase diagram of two-component interacting

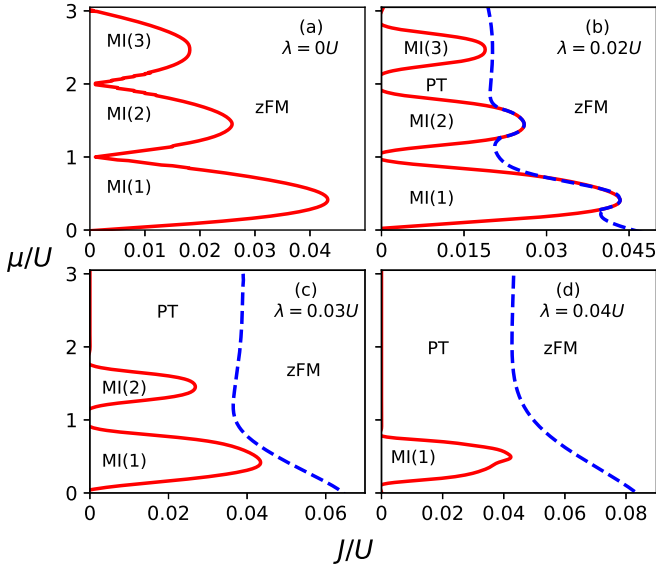


FIG. 6. The zero-temperature ground state phase diagram in the presence of Rashba SOC for various SOC strengths. The filling or occupancy of the Mott lobe is represented by  $n$  in  $\text{MI}(n)$ . The interspin interaction  $U_{\uparrow\downarrow} = 1.5U$ , and the values of  $\lambda$  in units of  $U$  are shown in the upper right corner of the plot. The superfluidity near the MI lobes is twisted in character while at higher  $J$  the system is in zFM state.

bosonic system in the absence of SOC. The phase diagram for  $U_{\uparrow\downarrow} = 1.5U$  at  $\lambda = 0$  is shown in Fig. 6(a). Above the phase separation criterion, at  $J = 0$ , the width of all MI lobes is  $\Delta\mu/U = 1$ . Moreover, the critical hopping of the  $\text{MI}(1)$ -SF transition in Fig. 6(a) becomes identical to the  $\text{MI}(2)$ -SF for  $U_{\uparrow\downarrow} < U$  case as shown in Fig. 2(a). The details of the quantum phase transitions as a function of  $U_{\uparrow\downarrow}$  for two-component interacting scalar-bosonic system is reported in our previous study [45]. In the phase-separated superfluid, the condensation occurs in one of the component only, and it resembles the zFM phase [12, 29]. We further examine the SOC-driven superfluid phases and their parameter space as  $\lambda$  varied. The phase diagram for three representative cases are shown in Fig. 6(b)-(d). At  $\lambda = 0.02U$ , for lower hopping strengths, the phase-modulated PT superfluid emerges between the insulating lobes as shown in Fig. 6(b). For the phase-separated regime, the uniform occupancy of PT state is observed for  $n_i = n_{i\uparrow} + n_{i\downarrow}$  and the phase of each component varies diagonally as shown in Fig. 3(a). Further increase in  $J$  results into a transition to zFM superfluid. The effects of SOC at higher strengths  $\lambda = 0.03U$  and  $\lambda = 0.04U$  are shown in Figs. 6(c) and (d). At  $\lambda = 0.03U$ , the  $\text{MI}(3)$  completely vanishes, and the parameter regime of PT superfluid is enhanced. This is also evident from the SF region between the  $\text{MI}(1)$  and  $\text{MI}(2)$  lobes. At  $\lambda = 0.04U$ , the destruction of Mott lobes is enhanced as indicated by the absence of  $\text{MI}(2)$ . As SOC strength increases, the melting of insulating lobes occurs first for higher density lobes and then it continues to the lower ones. In addition, the  $J_c$  of  $\text{MI}$ -SF transition also decreases with  $\lambda$ . We find that at higher  $\lambda \approx 0.065U$ ,

the  $\text{MI}(1)$  phase gets completely destroyed and the system exhibits superfluid phase transition between PT and zFM states. The transition between the PT and zFM is a broad one. To get the phase boundary for this transition, we have used the non-linear least squares fitting and the residuals is of the order of  $10^{-3}$ . It is important to note that for stronger interspin interaction,  $U_{\uparrow\downarrow}/U > 1$ , we do not observe the ST phase. This is consistent with the quantum phases of continuum system with SOC where the tuning of Raman coupling for strong interspin interaction does not lead to ST phase [43].

### C. Finite temperature results for $U_{\uparrow\downarrow} = 0.5$

At finite temperature, the Mott lobe melts into NF phase due to thermal fluctuations. The NF phase has no long-range order, but it is compressible ( $\kappa \neq 0$ ). Therefore, this phase can be distinguished from the insulating MI phases by finite  $\kappa$ . We examine the melting of MI phase as a function of temperature for various SOC strengths. In Fig. 7, we plot the width of the first Mott lobe  $\text{MI}(1)$  at  $J = 0.01U$  for different values of  $\lambda$ . For  $\lambda = 0$ , at lower temperatures, the width of the MI lobe first increases for  $k_B T/U < 0.004$ .

At  $k_B T/U \approx 0.004$  the Mott lobe starts melting and width of the lobe decreases with temperature. At  $k_B T/U \approx 0.046$ , the MI phase is completely replaced by NF phase. However, for finite  $\lambda$ , there is a combined effect of SOC and finite temperature on the width of the Mott lobe. For  $\lambda = 0.02U$ , at low temperatures the width first increases then at  $k_B T/U \approx 0.009$  the thermal fluctuations overcome the SOC effects, and this leads to decrease in the width. The effects of SOC are prominent at larger values of  $\lambda$  as evident for  $\lambda = 0.03U$  and  $0.04U$  cases in Fig. 7. At higher temperatures, the melting of MI phase is independent of  $\lambda$ , and the decrease in the width of MI lobe is similar to  $\lambda = 0$  case.

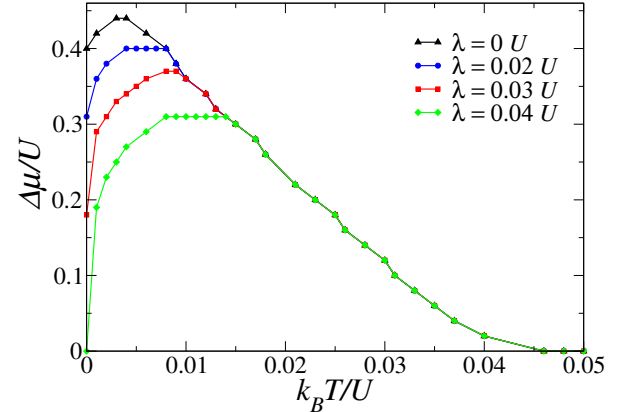


FIG. 7. The width of first Mott lobe  $\text{MI}(1)$  at  $J = 0.01U$  as a function of temperature for various SOC strengths. The values of  $\lambda$  in units of  $U$  are shown in the upper right corner of the plot. Here, the interspin interaction  $U_{\uparrow\downarrow} = 0.5U$ . At lower temperatures, the melting of the MI lobe depends on the value of  $\lambda$ , and at higher  $k_B T$  the width remains similar to  $\lambda = 0$  case. For all cases, with and without SOC, the  $\text{MI}(1)$  phase completely melts and replaced by NF phase at  $k_B T/U \approx 0.046$ .

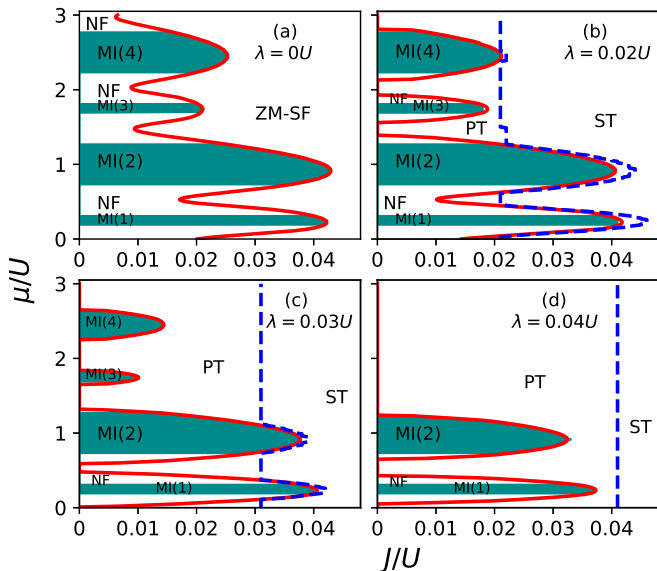


FIG. 8. The finite temperature phase diagram of BHM for different values of  $\lambda$  at  $k_B T/U = 0.03$ . The interspin interaction  $U_{\uparrow\downarrow} = 0.5U$ . The shaded green bands are the insulating MI regions which is distinguished from NF phase present at finite  $T$ . The reemergence of insulating regimes and destruction of PT superfluidity at finite temperatures are observed. The constant width of MI(1) for both zero and finite SOC confirms the behaviour reported in Fig. 7. The blue dashed line represents the PT-ST superfluid phase transition obtained using finite-temperature Gutzwiller mean-field approach.

We further discuss the finite temperature phase diagram at  $k_B T/U = 0.03$ , and it is shown in Fig. 8. At  $\lambda = 0$ , the thermal fluctuations destroy the off-diagonal long-range order of SF phase, and extend the parameter space of NF phase. Odd Mott lobes stretch along  $J/U$  axis. For example, at  $k_B T = 0$ , the critical hopping of MI(1)-SF transition is 0.0268 in Fig. 2(a) and at  $k_B T/U = 0.03$  it increases to 0.0422 as evident from Fig. 8(a). Similar enhancement is also apparent for MI(3) from the comparison of Figs. 8(a) and 2(a). In the presence of SOC, there is an interplay of the effects of SOC and finite temperature. For smaller SOC strengths ( $\lambda = 0.02$  and  $0.03$ ), the remarkable feature of the reemergence of MI lobes at the cost of finite-momentum superfluids at finite temperature is observed. In particular, the SOC-induced PT phase near the atomic limit in Fig 2(b) melts into MI(3) and NF phases as shown in Fig. 8(b). The destruction of PT superfluidity with a wide region of NF state at finite temperatures is consistent with the previous Monte Carlo study of strongly-correlated bosons with SOC [28]. The reemergence of insulating domains at finite temperature is in agreement with our analysis of the width of MI lobe with SOC which is shown in Fig. 7. While increasing the SOC strengths from 0.02 [Fig. 8(b)] to 0.03 [Fig. 8(c)], the PT state is favoured by melting the NF and MI phases. At  $\lambda = 0.04U$ , the phase boundary of PT to ST superfluid transition, as in the case of zero temperature, remains unchanged and independent of the average particle densities or  $\mu$  at finite temperatures.

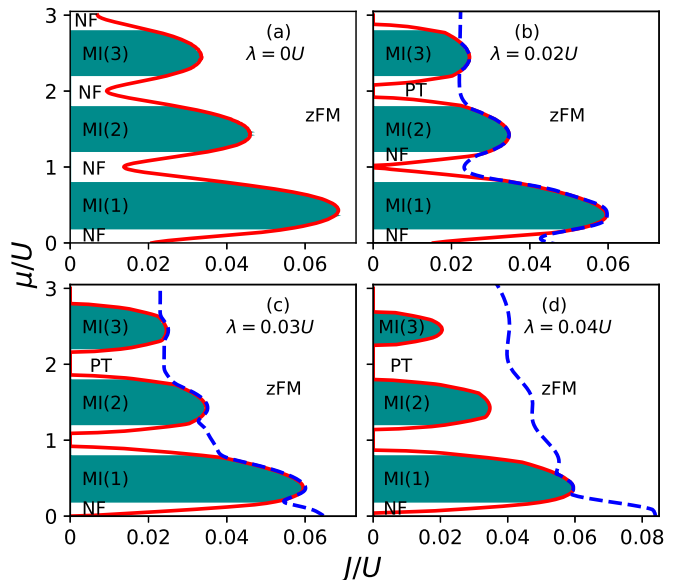


FIG. 9. The finite temperature phase diagram of BHM for different values of SOC strengths at  $U_{\uparrow\downarrow} = 1.5U$ . The shaded green bands represent the residual insulating domains in the presence of thermal fluctuations. Outside of the bands tiny white region shows NF phase. The thermal energy corresponding to temperature is  $k_B T/U = 0.03$ . The finite temperature stabilizes the MI phases against the SOC and suppress the finite-momentum superfluidity. This is evident from (c,d), as compared to corresponding zero temperature case shown in Figs. 6(c,d).

#### D. Finite temperature results for $U_{\uparrow\downarrow} = 1.5$

Like in the case of  $U_{\uparrow\downarrow} = 0.5U$ , we examine the finite-temperature phase diagram in the phase-separated regime with SOC. In particular, we explore the stability of the finite-momentum superfluids with the thermal fluctuations arising from finite  $T$ . To gain better insights, we briefly review the  $\lambda = 0$  case. As expected the insulating lobes melt to the NF phase at  $k_B T/U = 0.03$ , and this is discernible from the phase diagram shown in the Fig. 9(a). The phase diagrams of  $\lambda \neq 0$  at  $k_B T/U = 0.03$  are shown in the Fig. 9(b)-(d). At  $\lambda = 0.02U$ , the thermal fluctuations favour the insulating domains, and the emergence of NF phase between the MI lobes reduces the PT superfluidity as is evident from the comparison of Fig. 9(b) with Fig. 6(b). The reemergence of MI lobes at finite  $T$  is also there in this case as can be confirmed by comparing Figs. 9(c)-(d) with 6(c)-(d). At the phase boundaries, the critical hopping of the MI-zFM and PT-zFM transitions are shifted to higher  $J$  at finite temperature as compared to the critical  $J$  at zero temperature. The effect of increase in SOC strength leading to the increase in PT superfluid phase is also evident in the phase diagrams shown in the Figs. 9(c)-(d) similar to  $U_{\uparrow\downarrow}/U < 1$  case.



## V. CONCLUSIONS

We have studied the parameter domain of various finite-momentum superfluids of spin-orbit coupled ultracold bosonic atoms in two-dimensional optical lattices. To examine various superfluid states with different atomic densities and phase ordering, we have used spin-dependent momentum distributions, a routinely measured observable in cold-atom experiments. For  $U_{\uparrow\downarrow} < U$ , with  $\lambda/J \lesssim 1$  the favored superfluid phase is PT, whereas with  $\lambda/J \gtrsim 1$  the system is in ST phase. Starting with PT phase, the increase in  $J$ , results in PT to ST superfluid phase transition. We have further shown that the inclusion of the quantum fluctuations via cluster Gutzwiller approach results in  $ST_{\text{den}}$  phase corresponding to the parameter domain of ST phase obtained with Gutzwiller mean-field theory. In the limit,  $U_{\uparrow\downarrow} > U$ , the stripe superfluid is absent, and phase-twisted to  $z$ -polarized ferromagnetic transition is observed as  $J$  is varied. We have further shown that the thermal fluctuations destroy the phase-twisted superfluidity, and favour the insulating and normal states. The results of the present study are pertinent to the ongoing quantum gas experiments with spin-orbit coupling and offer a parameter space in the  $J - \mu$  plane to observe the novel finite-momentum superfluids.

## ACKNOWLEDGMENTS

We thank Deepak Gaur and Hrushikesh Sable for valuable discussions and acknowledge the support of High Performance Computing Cluster at IAMS, Academia Sinica, Taiwan. S.G. thanks Science & Engineering Research Board (SERB), Department of Science and Technology, Government of India (Project: ECR/2017/001436) for support.

### Appendix: Finite-temperature Gutzwiller mean-field theory

We incorporate the effects of the thermal fluctuations at finite temperatures by considering the thermal average of the

observable quantities. To compute the thermal average, we first get the full set of eigenspectrum obtained from the diagonalization of the mean-field Hamiltonian. We further use the single-site energy spectrum  $E_i^l$  and the eigenstates  $|\psi\rangle_i^l$  to evaluate the partition function of the system

$$Z_i = \sum_{l=1}^{N_b} e^{-\beta E_i^l}, \quad (\text{A.1})$$

where  $l$  is the eigenstate index,  $N_b$  is the Fock space dimension,  $\beta = (k_B T)^{-1}$ , and  $T$  is the temperature of the system. At finite  $T$ , the region of the phase diagram with vanishing SF order parameter and the real number occupancy  $\langle \hat{n}_{i\alpha} \rangle$  is defined as the normal-fluid state.

From the definition of the partition function, the thermal average of the SF order parameter is

$$\langle \phi_{i\alpha} \rangle = \frac{1}{Z} \sum_{l=0}^{N_b} \langle \psi | \hat{b}_{i\alpha} e^{-\beta E^l} | \psi \rangle_i^l, \quad (\text{A.2})$$

where  $\alpha = \uparrow, \downarrow$  is the spin-component index and  $\langle \dots \rangle$  represents the thermal averaging of  $\phi$ . Similarly, the atomic occupancy at finite  $T$  is defined as

$$\langle \langle \hat{n}_{i\alpha} \rangle \rangle = \frac{1}{Z} \sum_{l=0}^{N_b} \langle \psi | \hat{n}_{i\alpha} e^{-\beta E^l} | \psi \rangle_i^l. \quad (\text{A.3})$$

The average occupancy is  $\langle n_\alpha \rangle = \sum_i \langle \langle \hat{n}_{i\alpha} \rangle \rangle / L$ . At finite  $T$ , the spin-dependent momentum distributions  $\langle \rho_{\uparrow, \downarrow}(\mathbf{k}) \rangle$  are computed from the thermal-averaged SF order parameters.

- 
- [1] M. Z. Hasan and C. L. Kane, *Rev. Mod. Phys.* **82**, 3045 (2010).
  - [2] X.-L. Qi and S.-C. Zhang, *Rev. Mod. Phys.* **83**, 1057 (2011).
  - [3] A. Manchon, H. C. Koo, J. Nitta, S. M. Frolov, and R. A. Duine, *Nat. Mater.* **14**, 871 (2015).
  - [4] Z. F. Ezawa, *Quantum Hall Effects: Recent Theoretical and Experimental Developments*, 3rd ed. (World Scientific, Singapore, 2013).
  - [5] L. Balents, *Nature (London)* **464**, 199 (2010).
  - [6] X. Wan, A. M. Turner, A. Vishwanath, and S. Y. Savrasov, *Phys. Rev. B* **83**, 205101 (2011).
  - [7] I. Žutić, J. Fabian, and S. Das Sarma, *Rev. Mod. Phys.* **76**, 323 (2004).
  - [8] Z. Wu, L. Zhang, W. Sun, X.-T. Xu, B.-Z. Wang, S.-C. Ji, Y. Deng, S. Chen, X.-J. Liu, and J.-W. Pan, *Science* **354**, 83 (2016).
  - [9] W. Sun, B.-Z. Wang, X.-T. Xu, C.-R. Yi, L. Zhang, Z. Wu, Y. Deng, X.-J. Liu, S. Chen, and J.-W. Pan, *Phys. Rev. Lett.* **121**, 150401 (2018).
  - [10] S. Zhang and G.-B. Jo, *Journal of Physics and Chemistry of Solids* **128**, 75 (2019).
  - [11] J. Radić, A. Di Ciolo, K. Sun, and V. Galitski, *Phys. Rev. Lett.* **109**, 085303 (2012).
  - [12] W. S. Cole, S. Zhang, A. Paramakanti, and N. Trivedi, *Phys. Rev. Lett.* **109**, 085302 (2012).
  - [13] Y.-J. Lin, K. Jiménez-García, and I. B. Spielman, *Nature* **471**, 83 (2011).
  - [14] J. Li, W. Huang, B. Shteynas, S. Burchesky, F. C. Top, E. Su, J. Lee, A. O. Jamison, and W. Ketterle, *Phys. Rev. Lett.* **117**, 185301 (2016).
  - [15] J.-R. Li, J. Lee, W. Huang, S. Burchesky, B. Shteynas, F. C.

- Top, A. O. Jamison, and W. Ketterle, *Nature* **543**, 91 (2017).
- [16] V. Galitski and I. B. Spielman, *Nature* **494**, 49 (2013).
- [17] S.-C. Ji, J.-Y. Zhang, L. Zhang, Z.-D. Du, W. Zheng, Y.-J. Deng, H. Zhai, S. Chen, and J.-W. Pan, *Nature Physics* **10**, 314 (2014).
- [18] Z. Cai, X. Zhou, and C. Wu, *Phys. Rev. A* **85**, 061605(R) (2012).
- [19] M. Gong, Y. Qian, M. Yan, V. W. Scarola, and C. Zhang, *Scientific Reports* **5**, 10050 (2015).
- [20] A. T. Bolukbasi and M. Iskin, *Phys. Rev. A* **89**, 043603 (2014).
- [21] D. Yamamoto, I. B. Spielman, and C. A. R. Sá de Melo, *Phys. Rev. A* **96**, 061603(R) (2017).
- [22] M. Yan, Y. Qian, H.-Y. Hui, M. Gong, C. Zhang, and V. W. Scarola, *Phys. Rev. A* **96**, 053619 (2017).
- [23] T. Graß, K. Saha, K. Sengupta, and M. Lewenstein, *Phys. Rev. A* **84**, 053632 (2011).
- [24] S. Mandal, K. Saha, and K. Sengupta, *Phys. Rev. B* **86**, 155101 (2012).
- [25] P. Soltan-Panahi, D.-S. Luhmann, J. Struck, P. Windpassinger, and K. Sengstock, *Nat. Phys.* **8**, 71 (2012).
- [26] C. Hamner, Y. Zhang, M. A. Khamsehchi, M. J. Davis, and P. Engels, *Phys. Rev. Lett.* **114**, 070401 (2015).
- [27] T. M. Bersano, J. Hou, S. Mossman, V. Gokhroo, X.-W. Luo, K. Sun, C. Zhang, and P. Engels, *Phys. Rev. A* **99**, 051602(R) (2019).
- [28] C. Hickey and A. Paramekanti, *Phys. Rev. Lett.* **113**, 265302 (2014).
- [29] A. Dutta, A. Joshi, K. Sengupta, and P. Majumdar, *Phys. Rev. B* **99**, 195126 (2019).
- [30] Y. Zhang, G. Chen, and C. Zhang, *Scientific Reports* **3**, 1937 (2013).
- [31] M. C. Gutzwiller, *Phys. Rev. Lett.* **10**, 159 (1963).
- [32] D. S. Rokhsar and B. G. Kotliar, *Phys. Rev. B* **44**, 10328 (1991).
- [33] W. Krauth, M. Caffarel, and J.-P. Bouchaud, *Phys. Rev. B* **45**, 3137 (1992).
- [34] K. Sheshadri, H. R. Krishnamurthy, R. Pandit, and T. V. Ramakrishnan, *EPL* **22**, 257 (1993).
- [35] C. Menotti, C. Trefzger, and M. Lewenstein, *Phys. Rev. Lett.* **98**, 235301 (2007).
- [36] M. Iskin, *Phys. Rev. A* **83**, 051606(R) (2011).
- [37] S. Bandyopadhyay, R. Bai, S. Pal, K. Suthar, R. Nath, and D. Angom, *Phys. Rev. A* **100**, 053623 (2019).
- [38] K. Suthar, R. Kraus, H. Sable, D. Angom, G. Morigi, and J. Zakrzewski, *Phys. Rev. B* **102**, 214503 (2020).
- [39] Y. Kuno, K. Shimizu, and I. Ichinose, *Phys. Rev. A* **95**, 013607 (2017).
- [40] R. Bai, S. Bandyopadhyay, S. Pal, K. Suthar, and D. Angom, *Phys. Rev. A* **98**, 023606 (2018).
- [41] S. Pal, R. Bai, S. Bandyopadhyay, K. Suthar, and D. Angom, *Phys. Rev. A* **99**, 053610 (2019).
- [42] K. Suthar, H. Sable, R. Bai, S. Bandyopadhyay, S. Pal, and D. Angom, *Phys. Rev. A* **102**, 013320 (2020).
- [43] L. Chen, H. Pu, Z.-Q. Yu, and Y. Zhang, *Phys. Rev. A* **95**, 033616 (2017).
- [44] P. Buonsante and A. Vezzani, *Phys. Rev. A* **70**, 033608 (2004).
- [45] R. Bai, D. Gaur, H. Sable, S. Bandyopadhyay, K. Suthar, and D. Angom, *Phys. Rev. A* **102**, 043309 (2020).
- [46] D. Yamamoto, T. Ozaki, C. A. R. Sá de Melo, and I. Danshita, *J. Low Temp. Phys.* **175**, 258 (2013).
- [47] D. Yamamoto, T. Ozaki, C. A. R. Sá de Melo, and I. Danshita, *Phys. Rev. A* **88**, 033624 (2013).
- [48] Y. Kato, D. Yamamoto, and I. Danshita, *Phys. Rev. Lett.* **112**, 055301 (2014).
- [49] G.-H. Chen and Y.-S. Wu, *Phys. Rev. A* **67**, 013606 (2003).